Renewable Energy 81 (2015) 442–456

Contents lists available at ScienceDirect

Renewable Energy

journal homepage: www.elsevier.com/locate/renene

Combining wave energy with wind and solar: Short-term forecasting

Gordon Reikard [a, *], Bryson Robertson [b], Jean-Raymond Bidlot [c]

[a] Statistics Department, U.S. Cellular®, USA
[b] University of Victoria, Canada
[c] European Center for Medium-Range Weather Forecasts, UK

ARTICLE INFO

Article history:
Received 13 December 2014
Accepted 12 March 2015
Available online

Keywords:
Wave energy
Wind power
Solar power
Forecasting
Grid integration

ABSTRACT

While wind and solar have been the leading sources of renewable energy up to now, waves are increasingly being recognized as a viable source of power for coastal regions. This study analyzes integrating wave energy into the grid, in conjunction with wind and solar. The Pacific Northwest in the United States has a favorable mix of all three sources. Load and wind power series are obtained from government databases. Solar power is calculated from 12 sites over five states. Wave energy is calculated using buoy data, simulations of the ECMWF model, and power matrices for three types of wave energy converters. At the short horizons required for planning, the properties of the load and renewable energy are dissimilar. The load exhibits cycles at 24 h and seven days, seasonality and long-term trending. Solar power is dominated by the diurnal cycle and by seasonality, but also exhibits nonlinear variability due to cloud cover, atmospheric turbidity and precipitation. Wind power is dominated by large ramp events —irregular transitions between states of high and low power. Wave energy exhibits seasonal cycles and is generally smoother, although there are still some large transitions, particularly during winter months. Forecasting experiments are run over horizons of 1–4 h for the load and all three types of renewable energy. Waves are found to be more predictable than wind and solar. The forecast error at 1 h for the simulated wave farms is in the range of 5–7 percent, while the forecast errors for solar and wind are 17 and 22 percent. Geographic dispersal increases forecast accuracy. At the 1 h horizon, the forecast error for large-scale wave farms is 39–49 percent lower than at individual buoys. Grid integration costs are quantified by calculating balancing reserves. Waves show the lowest reserve costs, less than half wind and solar.

© 2015 Elsevier Ltd. All rights reserved.

1. Introduction

While wind and solar have been the leading sources of renewable energy up to now, waves are increasingly being recognized as a viable source of power for coastal regions [1,2]. One of the major issues in integrating renewable energy into the grid is short-term forecasting. In the electric power industry, forecasts are used in operational planning, peak load matching, switching sources and planning for reserve usage, i.e., buffering against the uncertainty caused by deviations between supply and demand, and deviations between supply and forecasts. The horizons range from as little as a few minutes to several hours, but are typically short. This study analyzes integrating wave energy into the power grid, in conjunction with wind and solar. The goal is to quantify the relative costs associated with all three types of renewable energy.

The Pacific Northwest in the United States has a favorable mix of all three sources, as well as robust data sets. Load and wind power are published by the Bonneville Power Administration (BPA). Operating as a wholly-owned subsidiary of the U.S. Department of Energy, BPA's service territory includes Idaho, Oregon, Washington, and parts of Montana, California, Nevada, Utah and Wyoming. The bulk of BPA's generating capacity is hydroelectric, but as of 2013, some 4515 megawatts (MW) of wind capacity had been installed, with an additional 2500 MW planned for 2015 [3].

Solar power development has been less extensive, but plans are underway to install capacity in inland areas that have less precipitation and more continuous sunlight. Data sets for 25 solar stations, over five states, are publically available from the University of Oregon's solar radiation measurement laboratory [4].

The wave energy on the outer continental shelf off the coasts of Washington and Oregon has been estimated at 179 terawatts (TW) in deep water and 140 TW closer to the coast, although it is likely that only a fraction of this can be extracted [5]. A more realistic

* Corresponding author. Tel.: +1 773 399 8802.
E-mail address: Reikarsen@msn.com (G. Reikard).

http://dx.doi.org/10.1016/j.renene.2015.03.032
0960-1481/© 2015 Elsevier Ltd. All rights reserved.

number for the wave energy that could be generated with existing technologies is on the order of 500 MW. Data on the wave height and period is available for several buoy sites from the National Data Buoy Center, operated by the National Oceanographic and Atmospheric Administration [6]. Wave parameters over wider areas are simulated using the European Center for Medium-range Weather Forecasts model (ECMWF, 2015).

The organization of this study is as follows. Section 2 reviews the load, solar and wind data. The calculations for wave energy are presented in Section 3. The forecasting methodology is set out in Section 4. Forecasting tests and grid integration experiments are run in Sections 5–6. Section 7 concludes.

2. The load, wind and solar power

The database was compiled for January 1, 2012 through December 31, 2013, at an hourly resolution. The load, wind and solar data were converted to hourly from the original 5 min and 15 min values. Table 1 gives the sources.

Fig. 1 shows the load over the three month period January–March 2012. The load exhibits cycles at 24 h and 7 days, seasonal cycles at 12 months, and a long-term trend associated with the growth of the economy. The seasonal cycle peaks during the winter months. The amplitude of the 7-day cycles varies from week to week. There are occasional outliers, generally associated with weather events.

BPA's wind generating capacity currently includes 43 sites, with several more under development. Maps of operational and planned installations are available at the BPA website [3]. The majority have been located in the Columbia River gorge, with additional stations along the Oregon coast and further inland. The average wind power in 2013 was 1218 MW, or 27 percent of capacity. Fig. 2 shows the wind power series over the same three month interval. The most prominent feature in wind is large ramp events—irregular transitions between states of high and low power.

Of the 25 solar data sets, many had extensive missing values. Twelve sites which had complete observational records were used. These include six in Oregon, three in Idaho, and one each in Montana, Utah and Wyoming (see Table 1). Fig. 3 shows the locations on a map. The values for ground level irradiance are the global horizontal component, in watts per meter squared (W/m^2). All the generation is assumed photovoltaic, so that the power can be calculated as a ratio to irradiance. The ratio was set to 7.2 percent.

Irradiance reaching the ground is intermittent, due to the effects of cloud cover, atmospheric turbidity and precipitation. However, some of this variability can be mitigated by dispersing sites over wide areas. The power calculations were run for the individual sites, then aggregated and scaled up to simulate 500 MW of solar power. Fig. 4 shows the combined solar power series. There is a strong seasonal cycle in the solar data, which runs counter to the seasonal cycle in the load: solar power peaks during the summer months. The main feature at short horizons is the diurnal cycle. While the aggregate series is much smoother than the data at individual sites, there is still evidence of nonlinear variability: the amplitude of the cycle can change from day to day, while weather events can result is large changes in power over intervals of a few hours.

3. Calculating wave power

The primary source for the wave data is four buoys off the coasts of Washington and Oregon—Cape Elizabeth, the Columbia River Bar, Stonewall Banks and Umpqua. Table 1 provides the buoy identifiers, the latitude and longitude, the depth, the resolution, and the number of usable values. The buoy data sets all include the significant wave height (H_{St}), in meters, and the mean wave period (T_{Mt}), in seconds. Fig. 3 shows the buoy locations. Figs. 5–6 show the wave height and period at Cape Elizabeth. Missing values were interpolated using ECMWF model simulations.

The ECMWF wave model is a third-generation physics-based model [7]. Large-scale physics-based wave models have been in operation since the 1960s, and have been updated repeatedly since this time [8–12]. The ECMWF wave and atmospheric models have been coupled since June 1998. In third-generation models of this type, the major properties of the wave spectra are determined by the action balance equation. Let N denote the wave action density, equal to the energy density divided by the intrinsic frequency. Let t denote time, and x, y denote distance in the Cartesian coordinates. Let σ denote the intrinsic frequency and γ denote the wave propagation direction. Let C_g denote the wave action propagation speed in (x, y, σ, γ) space, and S denote the combined source and sink terms. In deep water, the three major components of S are the input by wind (S_{IN}), nonlinear wave–wave interactions (S_{NL}) and wave dissipation through white-capping (S_{WC}). The action balance equation can be expressed in the following form:

$$\partial N/\partial t + \partial C_{g,x}N/\partial x + \partial C_{g,y}N/\partial y + \partial C_{g,\sigma}N/\partial \sigma + \partial C_{g\gamma}N/\partial \gamma = S;\quad S = [(S_{IN}) + (S_{NL}) + (S_{WC})] \tag{1}$$

Since January 2010, the average resolution of the grids simulated by the wave model has been 28 square km. Hourly data from the short range forecasts were obtained from the ECMWF archive to produce continuous time series at the four buoy locations. Model fields were interpolated from the original grid to the buoy coordinates using a bilinear method. The simulated parameters were the significant wave height and the zero-crossing mean wave period, which shows the closest correlation with the mean wave period from the buoy data.

In most prior studies, the wave energy has been calculated using the flux. Letting g denote the acceleration caused by gravity (9.8086 m/s/s), and ρ denote the density of seawater (1025 kg/m^3), the flux (in kW/m) is given by:

$$E_{Ft} = \left[\left(g^2\rho/64\pi\right)H_{St}^2 T_{Mt}\right] \approx 0.491\left(H_{St}^2 T_{Mt}\right) \tag{2}$$

Some recent studies have proposed simulating a generic converter in which the power is proportional to the flux for lower values of the wave height, but levels off above a given threshold [13]. The procedure used here, however, is to calculate the power flow from three types of wave energy converters (WECs), an attenuator, a point absorber, and an oscillating device. There is an important difference between these and the generic converter: the wave energy is a nonlinear function of the wave height and period, rather than the wave height squared, typically rising in proportion to both parameters and then declining as a function of the period [14].

The Pelamis P2 device is an offshore converter, operating in depths greater than 50 m [15–18]. The machine consists of a series of semi-submerged cylindrical sections linked by hinged joints. The wave-induced motion causes hydraulic cylinders to pump high pressure oil through motors driving electrical generators. The Pelamis conversion matrix is given in Fig. 7. The maximum power generated by the converter is 750 kW, at wave heights greater than or equal to 5.5 m. The resolution of the matrix is 0.5 m for the wave height and 0.5 s for the wave period. The matrix was increased to a resolution of 0.1 m for the wave height, using linear interpolations.

Performance matrices for several other WECs have recently been published [19]. The floating heave buoy array is composed of

Table 1
The data.

Database and variables	Units	Location	Resolution	Elevation or depth, usable values
All data is for the period January 1, 2012 through December 31, 2013.				
1] The load				
Power load	Megawatts	BPA service area	5 min	
Source: Bonneville Power Administration (BPA) website (http://transmission.bpa.gov/Business/Operations/Wind/).				
2] Wind power	Megawatts	43 wind farms	5 min	
Source: Bonneville Power Administration (BPA) website (http://transmission.bpa.gov/Business/Operations/Wind/).				
3] Solar				
Ashland, OR	Watts/m^2	42.19 N, 122.71 W	15 min	Elevation: 595 m
Burns, OR	Watts/m^2	43.52 N, 119.02 W	15 min	Elevation: 1295 m
Challis, ID	Watts/m^2	44.45 N, 114.31 W	15 min	Elevation: 1651 m
Dillon, MT	Watts/m^2	45.21 N, 112.62 W	15 min	Elevation: 1590 m
Eugene, OR (two series)	Watts/m^2	44.05 N, 123.07 W	15 min	Elevation: 150 m
Green River, WY	Watts/m^2	41.46 N, 109.44 W	15 min	Elevation: 1000 m
Hermiston, OR	Watts/m^2	45.82 N, 119.28 W	15 min	Elevation: 180 m
Moab, UT	Watts/m^2	38.58 N, 109.54 W	15 min	Elevation: 1000 m
Picabo, ID	Watts/m^2	43.31 N, 114.17 W	15 min	Elevation: 1472 m
Silver Lake, OR	Watts/m^2	43.31 N, 121.06 W	15 min	Elevation: 1355 m
Twin Falls, ID	Watts/m^2	42.55 N, 114.35 W	15 min	Elevation: 1200 m
Source: University of Oregon's solar radiation measurement laboratory (http://solardata.uoregon.edu).				
4] Waves				
NDBC 46041, Cape Elizabeth	Wave height, meters	47.35 N, 124.73 W	Hourly	Depth: 114.3 m
	Wave period, seconds			Usable values: 17,241
NDBC 46029, Columbia River bar	Wave height, meters	46.14 N, 124.51 W	Hourly	Depth: 135.3 m
	Wave period, seconds			Usable values: 10,941
NDBC 46050, Stonewall Banks	Wave height, meters	44.64 N, 124.53 W	Hourly	Depth: 128.1 m
	Wave period, seconds			Usable values: 17,491
NDBC 46229, Umpqua	Wave height, meters	43.77 N, 124.55 W	30 min	Depth: 187.1 m
	Wave period, seconds			Usable values: 17,126
Waves: National Data Buoy Center: www.ndbc.noaa.gov				

several heaving buoys connected to a submerged reference structure via a hydraulic system, which generates the electricity. In the conversion matrix (Fig. 8), the number of buoys was limited to ten, yielding a maximum power of slightly over 3600 kW. The floating three-body oscillating flap device consists of hinged flaps, which are all connected to a common frame. The matrix is given in Fig. 9. The maximum power is 1665 kW.

A second issue in wave farm simulation is geographic dispersal. Wave buoy data is known to show a great deal of localized noise. Recent papers have determined that the variance is substantially reduced when multiple converters are placed in the same area [20]. In this study, one converter is assumed to be located at the buoy site, so that the actual data can be used. The other converters are assumed to be deployed in a line and spaced roughly 150 m apart, so that there are 34 converters for every 5 km interval. The data sets for the locations other than the buoy are calculated by overlaying noise processes on the ECMWF model simulations. To estimate the noise process at the buoy site, the wave height and period data were smoothed using a centered 6 h moving average. The smoothed series were then subtracted from the actual data. The wave height noise exhibits strong evidence of seasonality: the tails are much thicker during the winter than during the summer. The

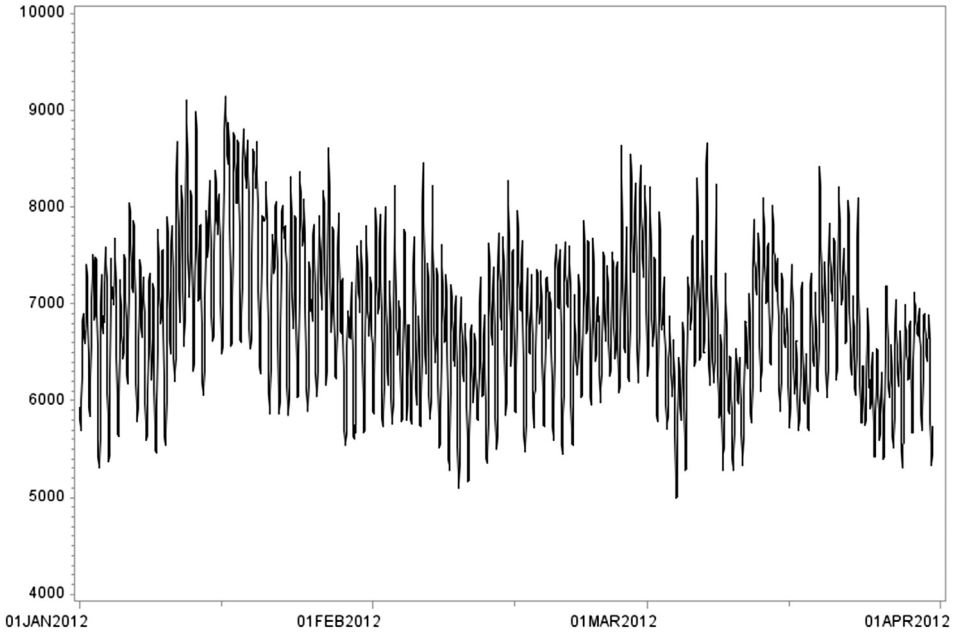

Fig. 1. The load, Bonneville Power Administration. Left scale: MW. January 1, 2012 to March 31, 2012.

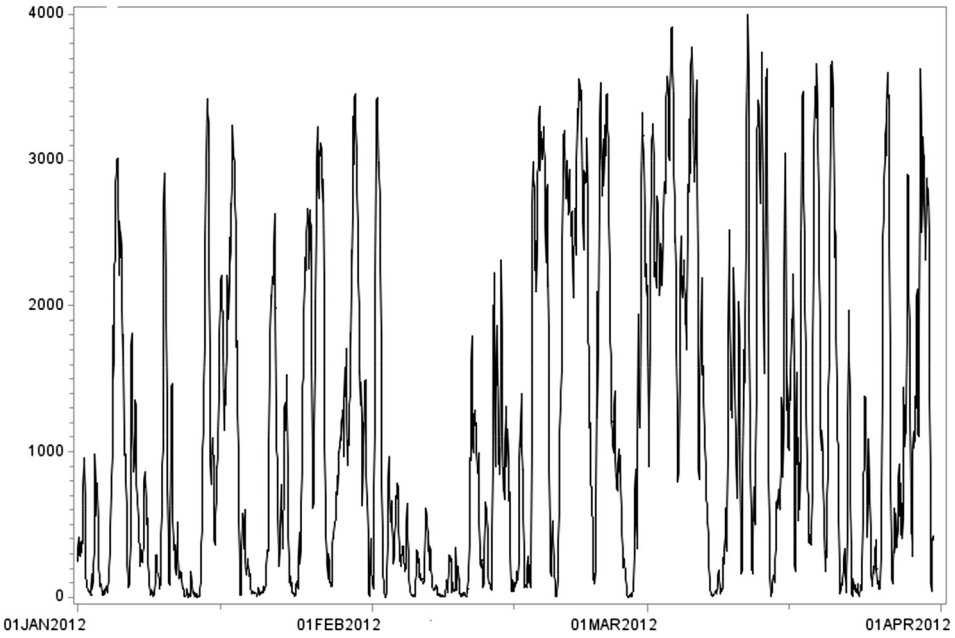

Fig. 2. Wind power, Bonneville Power Administration. Left scale: MW. January 1, 2012 to March 31, 2012.

wave period noise is less seasonal, although there are more outliers than in the standard normal.

Preliminary experiments for the wave noise were run using draws from various probability distributions. No single distribution replicates the observed pattern in the wave height noise. Instead, the preferred procedure was a blend of two distributions, with heavier tails for the winter months. The noise processes that most closely approximated the winter wave height were draws from a Student-t distribution with 5 degrees of freedom. The wave height during the summer months also shows somewhat heavier tails than in the Gaussian normal. A student-t distribution with 29 degrees of freedom closely replicated the observed values. The two noise series were then combined using seasonal weights. The distribution with 29 degrees of freedom also worked well for the wave period noise. Figs. 10–11 show simulated significant wave height and period series for Cape Elizabeth. Comparing these with the buoy data (Figs. 5–6), confirms that they have similar properties.

Finally, to create the wave farm simulations, the buoy data and the simulated H_{St} and T_{Mt} series were multiplied by the coefficients in the converter matrices. The main forecasting tests below are run for the 5 km wave farms, i.e., 34 converters. However, in the grid integration tests, larger wave farms had to be simulated. These were calculated by simulating additional

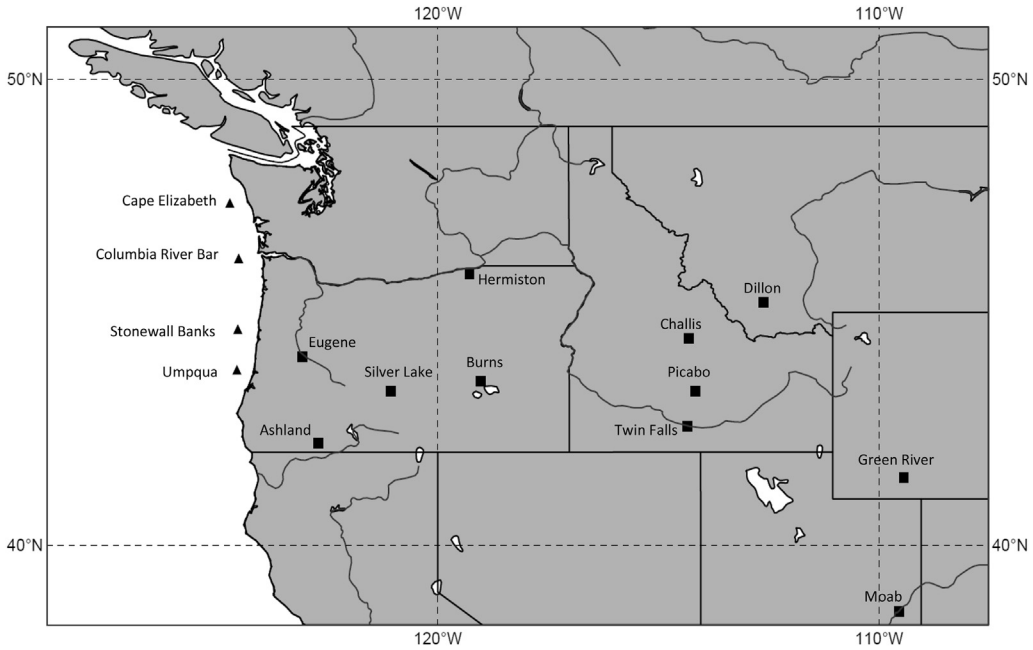

Fig. 3. The buoys and the solar stations. Triangles: wave buoys. Squares: solar sites.

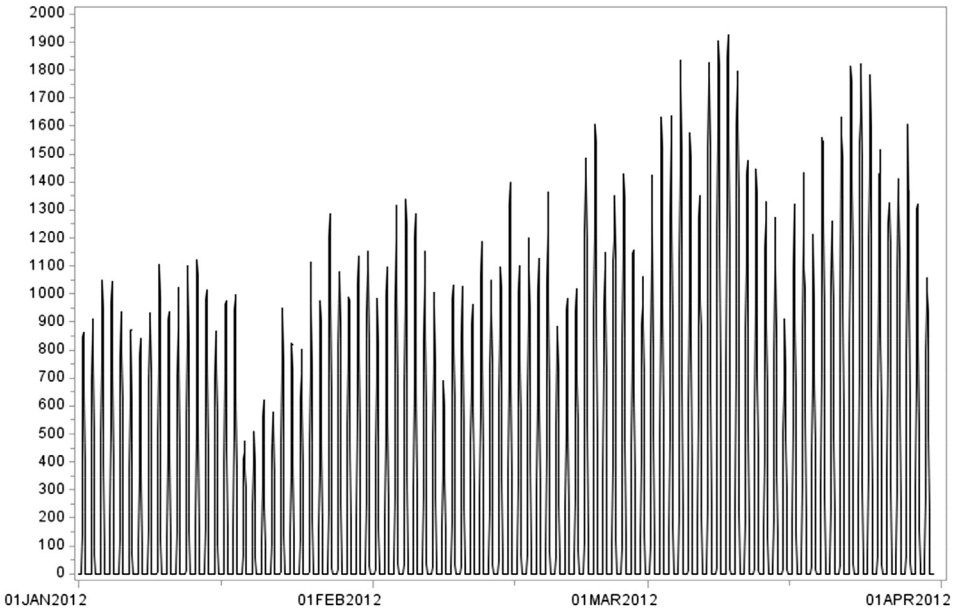

Fig. 4. Simulated solar power, 12 sites. Left scale: MW. January 1, 2012 to January 31, 2012.

converters over wider areas, and combining the power series at all four sites. To facilitate comparison, all the large wave farms were normalized to an average hourly power output of 500 MW.

Figs. 12–14 show the power series from the larger wave farms for the Pelamis, the heave buoy array and oscillating flap device. There are some visible differences between the simulated series. The Pelamis power series exhibits repeated transitions between states of high and low power, although within a narrower range than the other two converters. Even during the winter months, the power rarely exceeds 1900 MW. By comparison, the power series from the heave buoy array is considerably more volatile, with intermittent large spikes, and greater variability even during states of lower power. The series for the oscillating flap device is less volatile than the heave buoy array but still shows irregular sharp peaks, as well as fluctuations between states of low and intermediate power.

4. Forecasting methodologies

One issue that has arisen repeatedly in the wave literature is the choice of physics-based versus time series models. Physics models have been found to have good forecasting properties over longer horizons for waves [21–25]. However, over short horizons, time series models have often proven to be more accurate. Comparisons of physics and statistical methods have found that the convergence

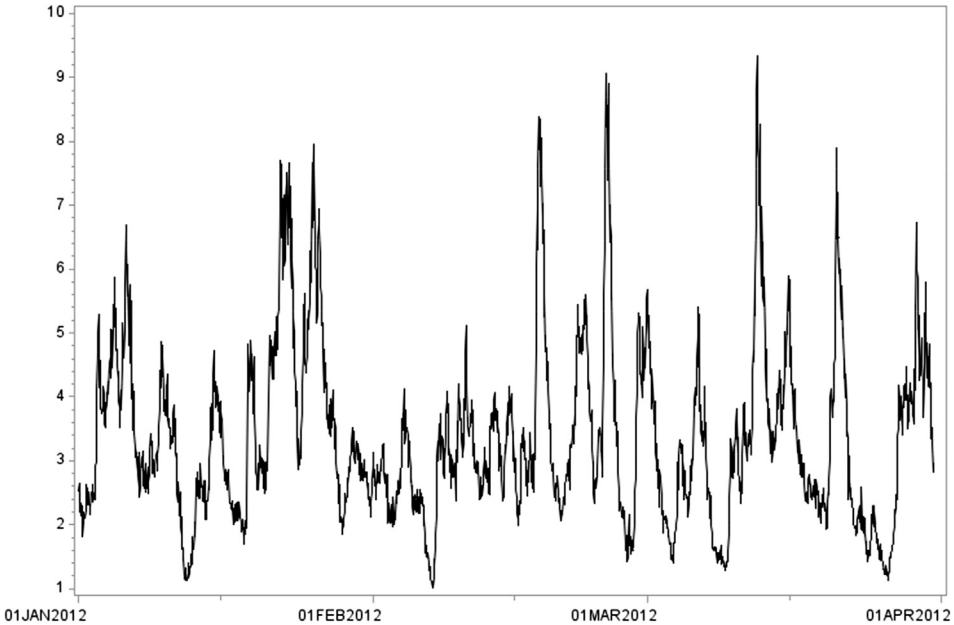

Fig. 5. Significant wave height, Cape Elizabeth. Left scale: Meters. January 1, 2012 to March 31, 2012.

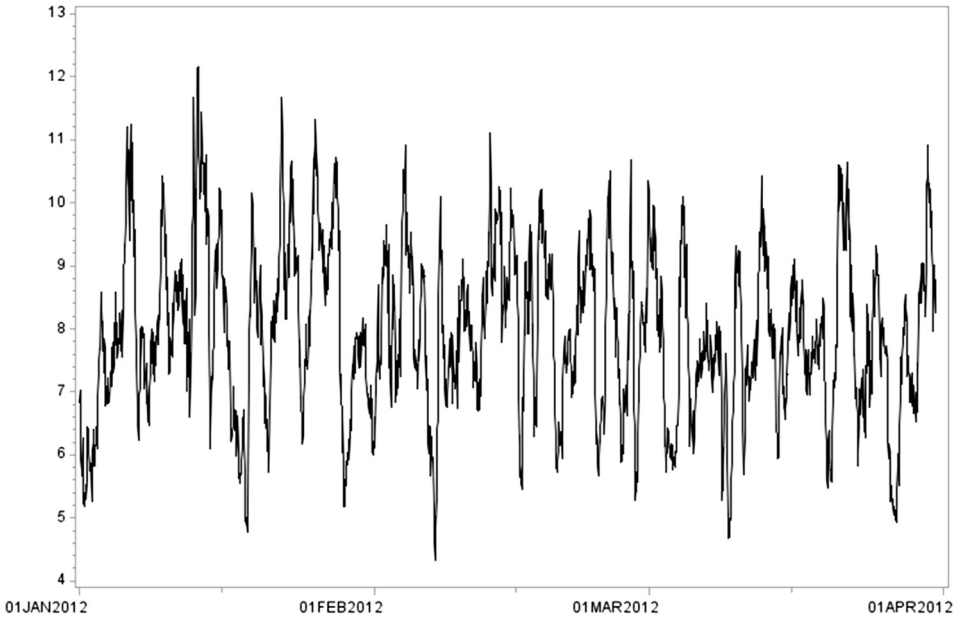

Fig. 6. Mean wave period, Cape Elizabeth. Left scale: seconds. January 1, 2012 to March 31, 2012.

point for waves, i.e., the horizon at which the two methods achieve comparable degrees of accuracy, is about 6 h [26,27]. For solar, the convergence time is probably shorter, on the order of 2 h [28,29]. The evidence on wind is limited, but time series models have generally been preferred at short intervals [30,31]. Consequently, the power production forecasts for all three types of renewable energy were run using time series models.

The basic model used here is regression with stochastic coefficients. Models of this type can capture a great deal of nonlinear variability [32,33]. Let Y_t denote a time series, let the resolution be

Signficant Wave Height (meters)	Wave Period (seconds) 5.0	5.5	6.0	6.5	7.0	7.5	8.0	8.5	9.0	9.5	10.0	10.5	11.0	11.5	12.0	12.5	13.0
1.0		22	29	34	37	38	38	37	35	32	29	26	23	21			
1.5	32	50	65	76	83	86	86	83	78	72	65	59	53	47	42	37	33
2.0	57	88	115	136	148	153	152	147	138	127	116	104	93	83	74	66	59
2.5	89	138	180	212	231	238	238	230	216	199	181	163	146	130	115	103	92
3.0	129	198	260	305	332	340	332	315	292	266	240	219	210	188	167	149	132
3.5		270	354	415	438	440	424	404	377	362	326	292	260	230	215	203	180
4.0			462	502	540	546	530	499	475	429	384	366	339	301	267	237	213
4.5			544	635	642	648	628	590	562	528	473	432	382	356	338	300	266
5.0				739	726	731	707	687	670	607	557	521	472	417	369	348	328
5.5				750	750	750	750	750	737	667	658	586	530	496	446	395	355
6.0					750	750	750	750	750	750	711	633	619	558	512	470	415
6.5					750	750	750	750	750	750	750	743	658	621	579	512	481
7.0						750	750	750	750	750	750	750	750	676	613	584	525
7.5							750	750	750	750	750	750	750	750	686	622	593
8.0								750	750	750	750	750	750	750	750	690	625

Fig. 7. Conversion matrix for the Pelamis P2 device. Power is in kilowatts.

Signficant Wave Height (meters)	Wave Period (seconds) 4	5	6	7	8	9	10	11	12	13	14	15	16
1.0	180	166	153	171	125	87	72	65	85	85	37	29	16
1.5	223	195	157	148	261	192	223	139	155	155	74	67	46
2.0			214	227	396	335	237	235	172	138	115	105	70
2.5				440	598	514	379	342	204	169	142	128	95
3.0				681	801	735	594	486	199	174	151	134	121
3.5				904	1035	949	788	617	239	209	183	164	146
4.0				1131	1269	1163	982	743	285	248	216	195	175
4.5				1358	1488	1374	1187	869	330	287	250	225	201
5.0				1585	1712	1585	1392	988	380	334	285	263	226
5.5				1812	1937	1798	2138	1107	429	381	323	301	261
6.0				2040	2162	2010	2884	1234	439	416	361	336	295
6.5				2267	2386	2221	3143	1360	449	450	406	372	329
7.0				2494	2611	2433	3619	1483	506	464	451	408	363

Fig. 8. Conversion matrix for the floating heave buoy array. Power is in kilowatts.

Signficant Wave Height (meters)	Wave Period (seconds)												
	4	5	6	7	8	9	10	11	12	13	14	15	16
1.0	19	29	47	57	52	37	29	20	17	13	9	7	7
1.5	42	63	92	111	109	65	56	38	29	22	19	13	11
2.0	66	99	151	201	165	105	85	59	52	41	29	24	19
2.5		160	242	262	226	166	118	83	70	57	39	39	26
3.0		213	319	372	327	211	152	116	94	75	66	45	42
3.5			436	503	408	293	203	148	115	93	75	58	44
4.0			554	540	521	355	261	192	144	123	84	81	56
4.5			645	746	587	379	302	236	190	154	106	90	74
5.0			796	926	695	486	341	287	211	168	136	111	94
5.5				955	808	603	430	343	231	201	150	120	97
6.0				1161	957	642	481	329	289	212	172	146	111
6.5				1476	1039	702	488	397	312	237	204	153	120
7.0				1665	1197	821	612	466	385	252	223	181	146

Fig. 9. Conversion matrix for the floating three-body oscillating flap device. Power is in kilowatts.

1 h, let ω denominate a coefficient, and let the subscript t denote time variation. The model is of the form:

$$\begin{aligned} \ln Y_t =& \omega_{0t} + \omega_{1t} \ln Y_{t-1} + \omega_{2t} \ln Y_{t-2} + \omega_{3t} \ln Y_{t-3} \\ &+ \omega_{4t} \ln Y_{t-4} + \varepsilon_t; \quad \varepsilon_t \sim P\left(0, \upsilon_t^2\right) \end{aligned} \tag{3}$$

where P is the probability distribution and υ_t^2 is the residual variance. Additional lags can be used as needed, but the Akaike information criterion favored limiting the lags to 4 h [34]. There was little evidence of any diurnal cycle in the wave data.

Neural networks have often been the preferred forecasting method for scientific time series. There is a vast literature on using neural networks to predict renewable energy [35–43]. The system architecture used here consists of a multilayer perceptron, trained using a backpropagation algorithm. For the time series analyzed below, the net was specified with three hidden layers, and one direct connection. It was trained by epoch, i.e., a forward and backward pass through all observations in the sample, rather than by example, i.e., a pass over individual observations. The input and bias weights were not retained from the previous period, but rather were restarted at each time point, so that in effect the weights are time-varying. The inputs to the neural net were the same as in the regressions.

When the data incorporate cycles at regular frequencies, as is the case with the load and solar power, ARIMA-type models have been found to be more effective than regressions on levels. Following the notation of Box and Jenkins [44], let $\phi(L)$ be the autoregressive operator, represented as a polynomial in the lag operator (L): $\phi(L) = 1 - \phi_1 L - \ldots - \phi_p L^p$. Let $\Phi(L)$ be the seasonal autoregressive operator. Let $\theta(L)$ be the moving average operator: $\theta(L) = 1 + \theta_1 L + \ldots + \theta_q L^q$, and $\Theta(L)$ be the seasonal moving average operator. Let the superscript ξ denote the order of differencing, and the superscript ζ denote the order of cyclical differencing. Let the superscript f denote the cyclical frequency. For hourly data, f = 24. The model is then of the form:

$$(1 - L)^{\xi}\left(1 - L^f\right)^{\zeta} \ln Y_t = [\theta_t(L)\Theta_t(L)/\phi_t(L)\Phi_t(L)]\varepsilon_t \tag{4}$$

The coefficients are again time-varying.

The forecasting experiments are set up as follows. The first 500 observations are used as a training sample. The power series are then forecasted iteratively. In each instance, the models are

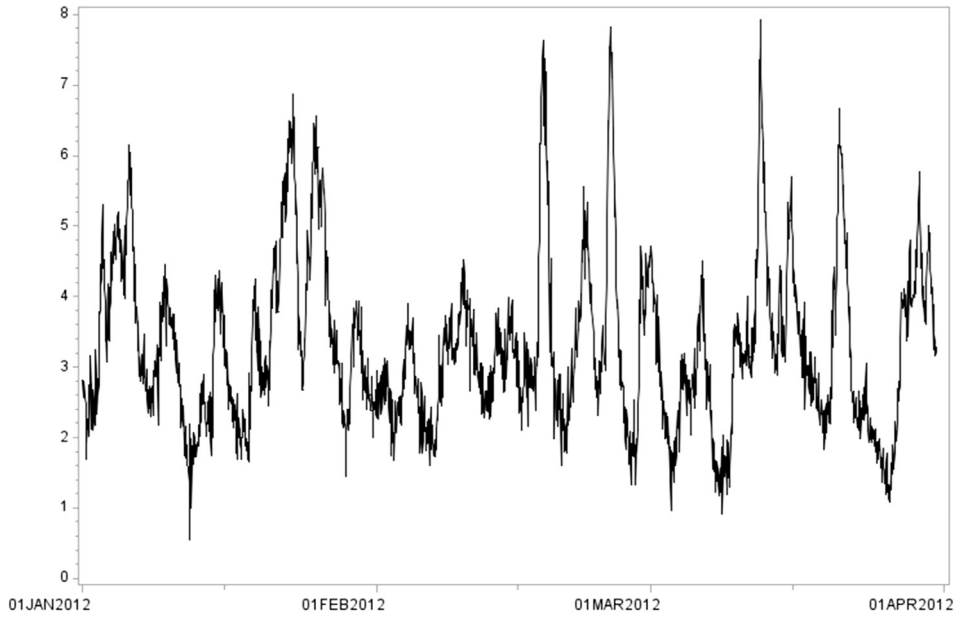

Fig. 10. Simulated significant wave height series, Cape Elizabeth. Left scale: Meters. January 1, 2012 to March 31, 2012.

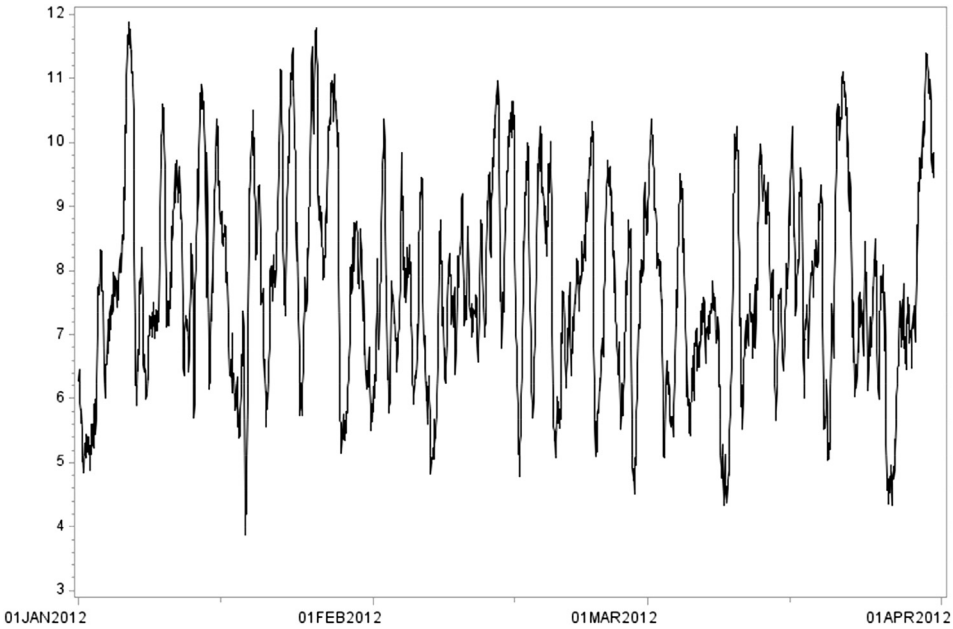

Fig. 11. Simulated mean wave period series, Cape Elizabeth. Left scale: seconds. January 1, 2012 to March 31, 2012.

estimated over prior values, forecasted, then re-estimated over the most recent value, etc. All the predictions are true out-of-sample forecasts, in that they use only data prior to the start of the forecast horizon. All the intervening periods are omitted. In other words, for horizon $t+2$, the forecasts for $t+1$ are excluded. The measure of forecast accuracy reported is the mean absolute percent error.

Time-varying parameter regressions can be estimated either using a Kalman filter [45] or a moving window. With an unrestricted Kalman filter, the coefficients behave as a random walk. This was found to impart too much volatility to the forecast values, reducing predictive accuracy. The choice is therefore between imposing restrictions on the filter, or varying the width of the moving window [46]. Several preliminary experiments were run. In most of the tests below, a width of 480 h is used.

5. Forecasting tests: initial findings

Table 2 presents the forecast error for the three types of renewable energy, the load and the net power, i.e., the load less the supply from wind, waves and solar. The tests are run for horizons of 1–4 h, although the main interest is the 1 h horizon. Table 3 reports the estimated coefficients.

5.1. Waves

The model is a regression on lags (Equation (3)). The neural network was also used for waves, but the results were extremely similar, so only the regression is reported. The forecasts were run both for the individual buoys, the 5 km wave farms, and the larger

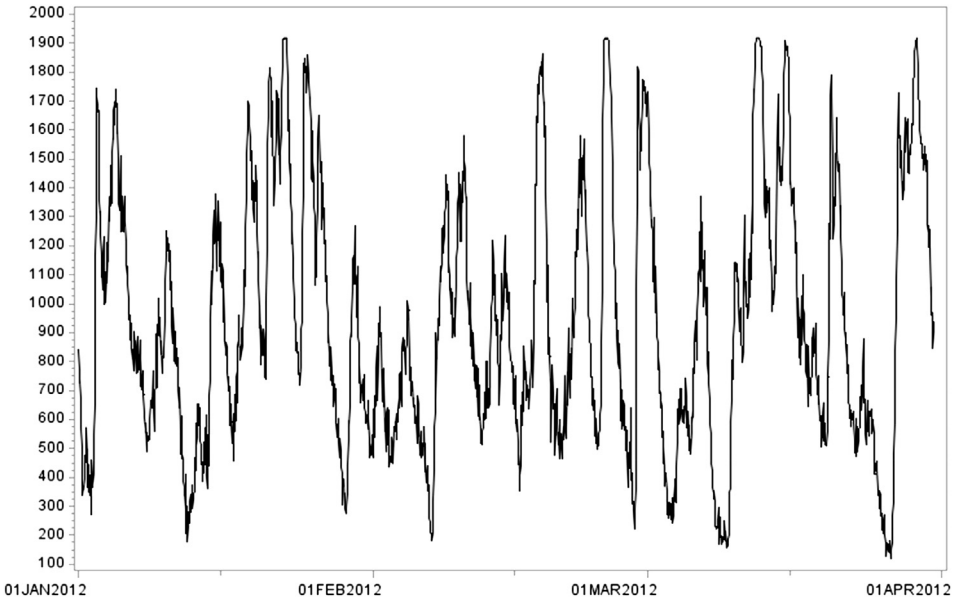

Fig. 12. Large wave farm simulation, Pelamis. Left scale: MW. January 1, 2012 to March 31, 2012.

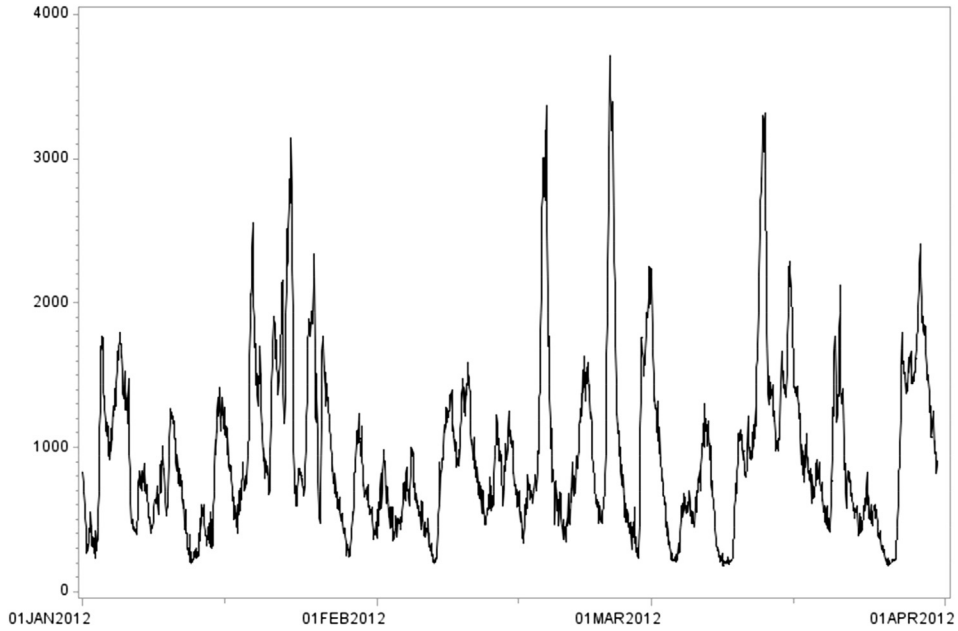

Fig. 13. Large wave farm simulation, heave buoy array. Left scale: MW. January 1, 2012 to March 31, 2012.

500 MW wave farms combining all four sites, for each type of device.

At Cape Elizabeth, the errors for the 5 km wave farm at the 1 h horizon range from 6.5 to 8.7 percent. At the Columbia River Bar, they range from 6.2 to 8.3 percent. At Stonewall Banks, they range from 6.2 to 8.5 percent. At Umpqua, they range from 6.3 to 8.6 percent. The heave buoy array shows the smallest errors, while the errors for the Pelamis and the oscillating flap device are usually fairly similar.

Averaging the four sites, the Pelamis shows errors of 10.2 percent for the individual buoys. This falls to 7.8 percent for the 5 km wave farms, and 5.9 percent when the four sites are combined. The forecast error is 23 percent lower at the 5 km wave farm than at the buoy, and 40 percent lower at the large wave farm.

The results for the heave buoy array show an even larger proportional improvement. The errors for the individual buoys average 11.08 percent. This declines to 6.3 percent at the 5 km wave farms, an improvement of 43 percent, and 5.2 percent at the combined wave farm, a reduction in the forecast error of 49 percent.

The oscillating flap device shows an average error of 11.44 percent for the individual buoys, and 8.54 percent for the 5 km wave farms, a proportional improvement of 25 percent. The error for the combined wave farm is 6.95 percent, or 39 percent lower than at the individual buoy sites.

As the horizon extends, the forecast errors increase, but the effects of geographic dispersal are still substantial. At 4 h, the

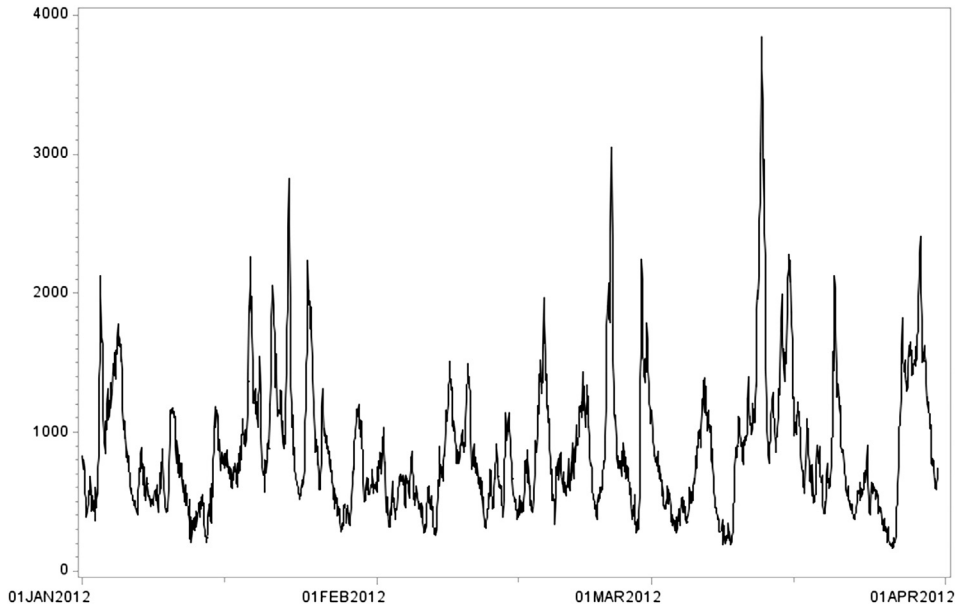

Fig. 14. Large wave farm power simulation, oscillating flap device. Left scale: MW. January 1, 2012 to March 31, 2012.

improvement in accuracy from the 5 km wave farms relative to the buoys is 28 percent for the Pelamis, 29 percent for the heave buoy array, and 22 percent for the oscillating flap device. The improvement from the combined wave farm relative to the buoys is 45 percent for the Pelamis, 43 percent for the heave buoy array, and 38 percent for the oscillating flap device.

5.2. Wind

The model for wind is also a regression, on three lags. Several other methods were also tried, including neural network and state transition models [47,48]. However, these failed to generate any improvement in accuracy with this data set. At the 1 h horizon, the best model for the wind power series shows an error of 22 percent. Forecast accuracy deteriorates sharply as the horizon extends. By 4 h, the wind error has increased to 76 percent.

5.3. Solar

There is an extensive literature on forecasting solar power using time series models [49,50]. The preferred method for this data set is an ARIMA (3,0,0) (2,1,0), i.e., three proximate lags, differencing at 24 h, and five lags corresponding to the 24 h cycle. As with waves, the forecast errors are reported both for the individual sites and for all sites combined. The errors are for daylight hours only; nighttime hours are excluded. At the individual sites, the errors range from a

Table 2
The forecast errors. Figures are the mean absolute percent error.

Variable	1 h	2 h	3 h	4 h
Waves				
Cape Elizabeth, 5 km wave farm, Pelamis	8.32	10.78	14.42	16.05
Cape Elizabeth, 5 km wave farm, heave buoy array	6.54	8.77	11.28	13.98
Cape Elizabeth, 5 km wave farm, oscillating flap device	8.74	11.76	14.93	17.31
Cape Elizabeth, buoy, Pelamis	12.01	15.19	18.44	21.59
Cape Elizabeth, buoy, heave buoy array	10.92	13.62	16.21	18.75
Cape Elizabeth, buoy, oscillating flap device	12.95	16.11	18.33	22.19
Columbia, 5 km wave farm, Pelamis	6.64	8.61	11.68	12.67
Columbia, 5 km wave farm, heave buoy array	6.23	8.44	11.61	12.81
Columbia, 5 km wave farm, oscillating flap device	8.32	11.38	14.24	16.95
Columbia, buoy, Pelamis	10.18	13.49	16.58	19.41
Columbia, buoy, heave buoy array	9.62	12.27	14.64	16.88
Columbia, buoy, oscillating flap device	11.51	14.88	17.91	20.66
Stonewall, 5 km wave farm, Pelamis	8.16	10.62	13.21	15.75
Stonewall, 5 km wave farm, heave buoy array	6.22	8.43	10.69	12.78
Stonewall, 5 km wave farm, oscillating flap device	8.49	11.27	14.08	16.72
Stonewall, buoy, Pelamis	12.85	15.86	18.96	21.89
Stonewall, buoy, heave buoy array	11.76	14.29	16.93	19.34
Stonewall, buoy, oscillating flap device	13.23	16.14	19.11	21.93
Umpqua, 5 km wave farm, Pelamis	8.19	10.53	13.06	15.84
Umpqua, 5 km wave farm, heave buoy array	6.31	8.45	10.13	12.74
Umpqua, 5 km wave farm, oscillating flap device	8.61	11.36	14.14	16.91
Umpqua, buoy, Pelamis	12.91	15.75	18.81	21.71
Umpqua, buoy, heave buoy array	12.04	14.65	17.15	19.58
Umpqua, buoy, oscillating flap device	14.06	17.11	19.98	22.67
Four sites combined, 500 MW wave farm, Pelamis	5.86	7.65	9.56	11.54
Four sites combined, 500 MW wave farm, heave buoy array	5.18	6.72	8.49	10.72
Four sites combined, 500 MW wave farm, oscillating flap device	6.95	9.01	11.21	13.42
Wind				
BPA Wind power series	22.09	42.16	58.13	77.25
Solar				
Ashland, OR	63.35	83.56	100.83	102.45
Burns, OR	65.83	87.78	106.34	108.92
Challis, ID	51.27	65.77	81.78	85.19
Dillon, MT	53.54	71.72	77.65	78.36
Eugene, OR	49.91	68.51	73.38	74.29
Eugene, OR (second series)	52.11	82.35	111.64	113.52
Green River, WY	62.58	85.24	89.85	91.82
Hermiston, OR	60.15	86.57	115.36	116.12
Moab, UT	58.27	72.04	86.45	88.21
Picabo, IA	46.52	62.86	70.19	71.79
Silver Lake, OR	61.94	78.06	84.57	89.91
Twin Falls, ID	44.01	56.75	61.48	63.59
All solar sites combined	16.98	23.15	30.20	31.35
Power load and net power				
Load	0.95	1.72	2.32	2.73
Net power (load less wind)	2.85	7.41	9.35	10.78
Net power (load less solar)	1.88	2.96	3.79	4.39
Net power (load less waves)				
Pelamis	1.21	2.06	2.74	3.26
Heave buoy array	1.36	2.24	2.96	3.47
Oscillating flap device	1.29	2.18	2.91	3.45

Notes: All series denominated in MW. The forecasts at 1–4 h horizons are run using data at a 1 h resolution. All calculations for solar, including net power, are for daylight hours only. All other calculations are for all time points.

Table 3
The model coefficients. Figures are regression coefficients. All coefficients are statistically significant at the 1 percent level or better.

RHS variable	Aggregate load	Solar	Wind	Waves (Pelamis)	Waves (heave buoy array)	Waves (oscillating flap device)
Constant	–	–	0.19	0.04	0.05	0.05
Lag, 1 h	1.45	0.98	1.43	0.84	0.85	0.82
Lag, 2 h	−0.61	−0.04	−0.54	0.33	0.29	0.31
Lag, 3 h	0.11	−0.07	0.13	0.20	0.01	0.02
Lag, 4 h	–	–	−0.05	−0.31	−0.19	−0.18
Lag, 24 h	−0.54	0.52	–	–	–	–
Lag, 48 h	−0.49	0.45	–	–	–	–
Lag, 72 h	−0.39	–	–	–	–	–
Lag, 96 h	−0.34	–	–	–	–	–
Lag, 120 h	−0.29	–	–	–	–	–
R-bar-square	0.991	0.994	0.963	0.989	0.987	0.995

Notes: the models for the load, wind and waves are run on natural logarithms, the model for solar is run on levels. The equations for the aggregate load and the solar power simulation are specified as ARIMA (5,0,0) (2,1,0) and ARIMA (3,0,0) (2,1,0), i.e., a regression on five or three proximate lags and two cyclical lags, in 24 h differences. The models for wind and waves are regressions on levels.

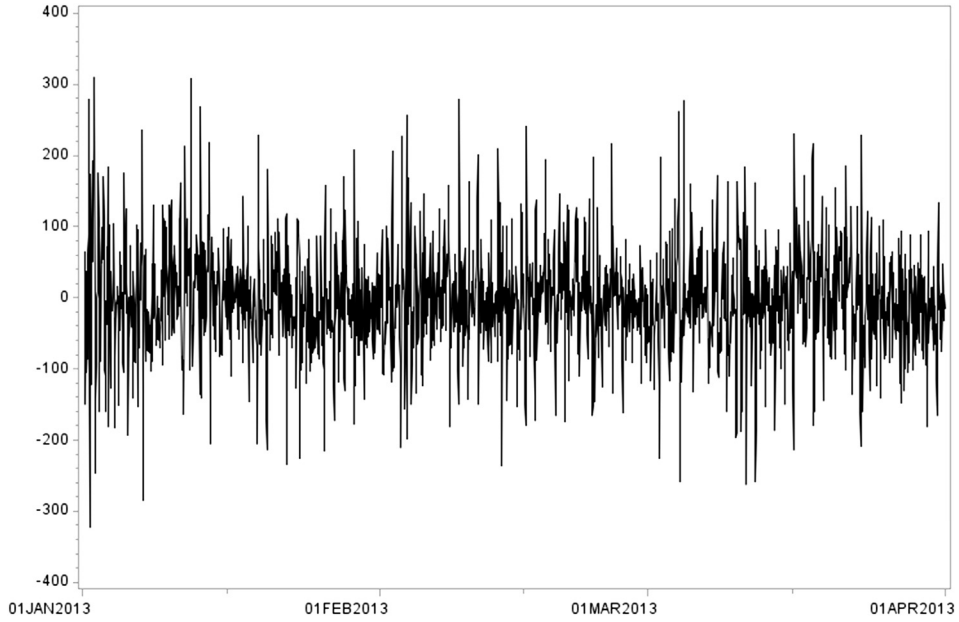

Fig. 15. The load forecast error. Left scale: MW. Forecast horizon: 1 h. January 1,2013 to March 31,2013.

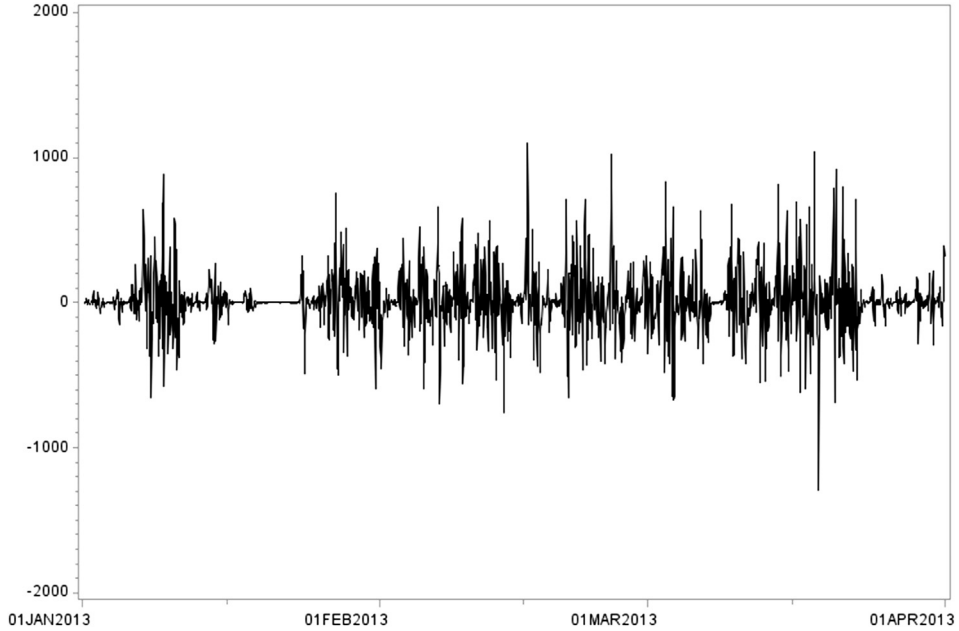

Fig. 16. The wind power forecast error. Left scale: MW Forecast horizon: 1 h. January 1, 2013 to March 31, 2013.

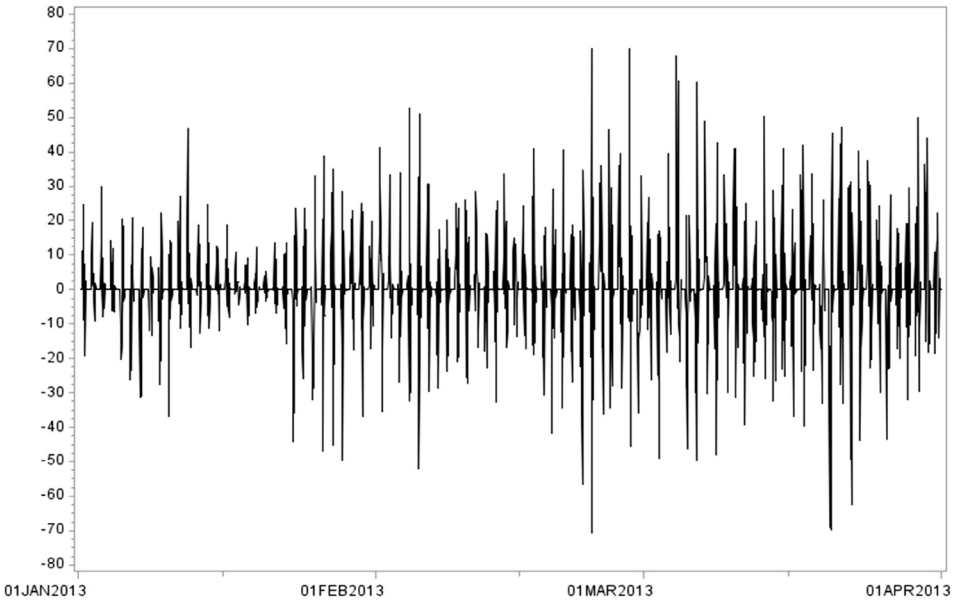

Fig. 17. The solar power forecast error. Left scale: MW. Forecast horizon: 1 h. January 1, 2013 to March 31, 2013.

minimum of 44 to a maximum of 72 percent at 1 h. The error increases sharply over 2–3 h, but then begins to level off around 4 h. Geographic dispersal does achieve a substantial improvement in predictability. The error for all the sites combined is 17 percent, increasing to 30.2 at 3 h and 31.3 percent at 4 h.

5.4. Load and net power

The load is forecasted using a two-stage model. The first is an ARIMA (3,0,0) (5,1,0), i.e., three proximate lags and lags over five 24 h intervals. In the second stage, the ARIMA forecast is used as an input in a neural network [51]. The forecast error for the load is very small, 0.95 percent at 1 h, rising to 2.73 percent at 4 h.

The forecasts for the net power use separate equations for the load and the renewable energy series. The net power associated with wind is substantially less predictable than the load: the error at 1 h is 2.85 percent, rising to over 10 percent at 4 h. The net power falls sharply during periods of high wind speed, when wind power approaches 40 percent of the load, but can rise just as rapidly when the wind dies down.

The net power errors associated with solar and waves are much smaller. However, these values are not strictly comparable to wind due to differences in scale (at 500 MW each, the mean wave and solar energy are less than half the mean wind energy of 1218 MW). The net power error for solar is 1.88 percent at 1 h and 4.39 percent at 4 h. For the three large wave farms, the net power errors are 1.21 for the Pelamis, 1.36 percent for the heave buoy array and 1.29 percent for the oscillating flap device. These increase to 3.24, 3.37 and 3.45 percent at 4 h.

While the mean absolute percent error is a widely-accepted gauge of model accuracy, the distribution of the error is also of interest. Figs. 15–20 present the errors for the load, wind, solar and waves, over a period of three months. The equation for the load tracks quite closely, with the error usually lower than 100 MW, and

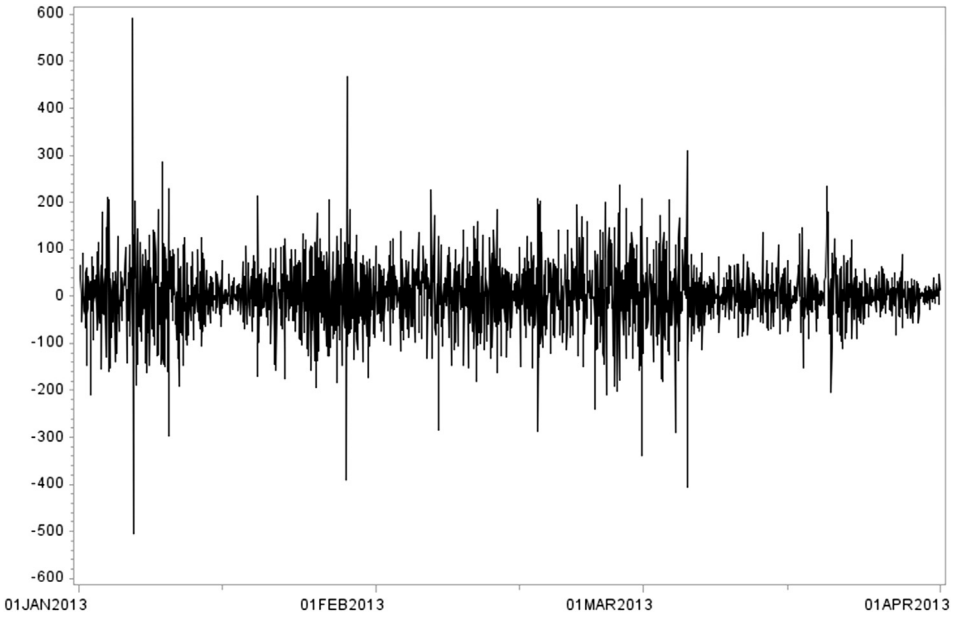

Fig. 18. The wave power forecast error, Pelamis. Left scale: MW. Forecast horizon: 1 h. January 1, 2013 to March 31, 2013.

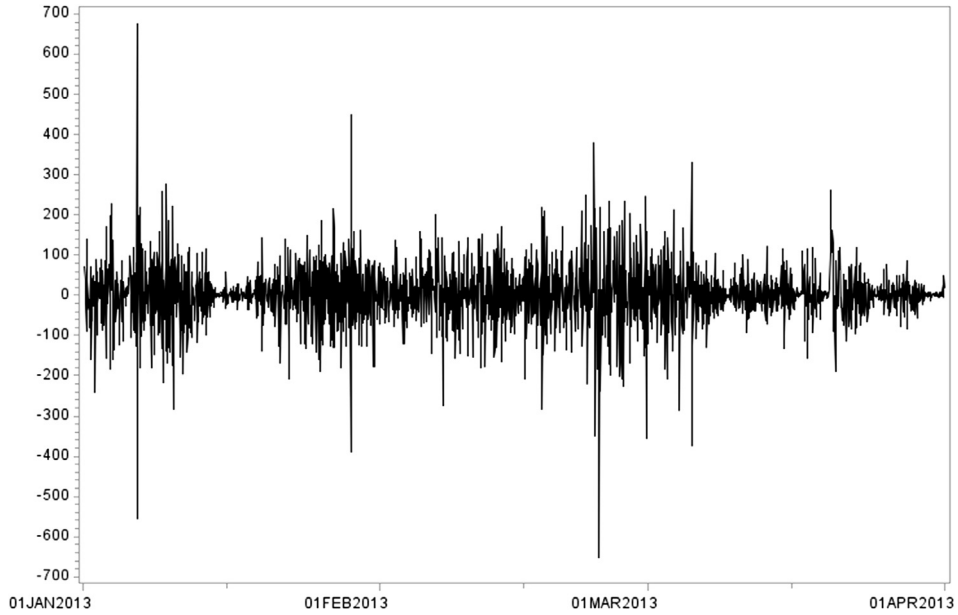

Fig. 19. The wave power forecast error, heave buoy array. Left scale: MW. Forecast horizon: 1 h. January 1, 2013 to March 31, 2013.

rarely exceeding 200 MW (2–3 percent of the load during the same interval). The wind forecast error shows much greater intermittency. The model alternates between periods of high accuracy and periods in which it goes seriously off, with errors in the range of several hundred MW. The solar power error also shows some intermittency, although it is considerably smaller than the wind error. The most interesting results are for waves, where the error is strongly seasonal. The wave error alternates among two main states. During the summer, the error is quite small. During the winter, the average error is higher, with occasional extreme outliers.

6. Reserve calculations

At BPA, there are three types of reserves. Regulation reserves cover differences between the supply and load within 10 min intervals, following reserves apply from one 10 min period to the next, while balancing reserves cover imbalances between forecast and supply at the 1 h horizon, with a 99.5 percent reliability requirement [3]. Capacity-up reserves are reserves associated with a deficit of energy relative to forecast. Capacity-down reserves are reserves associated with a surplus. The Federal Energy Regulatory Center (FERC) has also mandated 15 min transmission scheduling to assist in integrating variable sources [52]. Unfortunately, wave data is not available at the 15 min resolution. Consequently, the reserve calculations were run for the 1 h horizon.

Table 4 shows the reserves associated with the load, and each of the renewable energy sources, for the overall period, January 1, 2012 through December 31, 2013. However, reserves are not independent of scale, so the values are also expressed as a percent of power. For capacity down reserves, normally expressed as a negative number, the ratio is calculated using the absolute value.

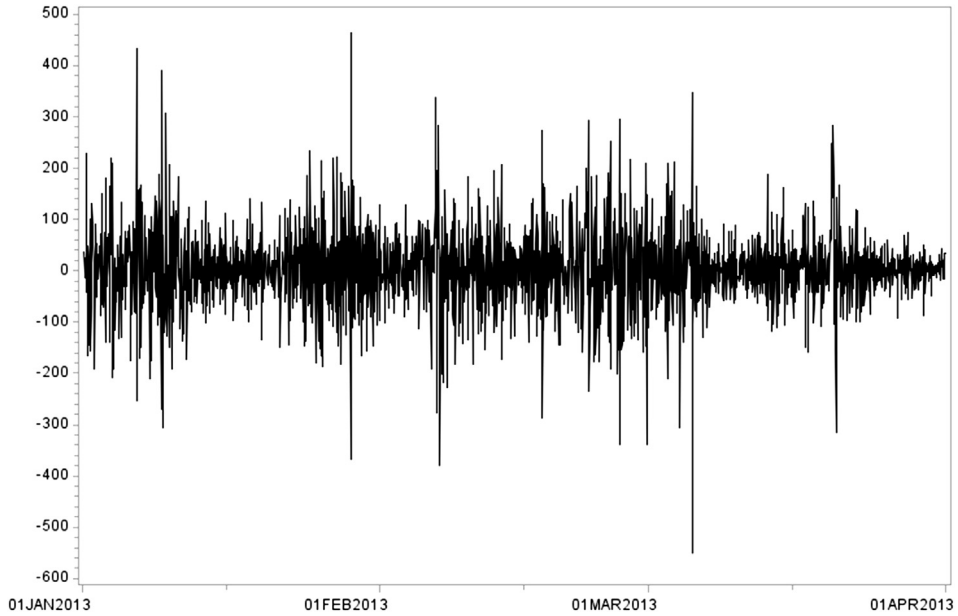

Fig. 20. The wave power forecast error, oscillating flap device. Left scale: MW. Forecast horizon: 1 h. January 1, 2013 to March 31, 2013.

Table 4
Balancing reserves. Statistics are the mean absolute value of reserves, and reserves as a percent of power.

Site and converter	Capacity up		Capacity down	
	Reserves (MW)	Reserves % of Power	Reserves (MW)	Reserves/Power Reserves % of Power
Aggregate load	58.98	0.93	−58.89	0.99
Wind (44 sites)	161.24	16.3	−94.54	37.1
Solar (12 sites)	67.06	15.2	−67.14	15.7
Waves (four sites)				
Pelamis	28.67	5.6	−25.32	5.9
Heaving converter	30.96	4.9	−26.63	5.2
Oscillating flap device	35.57	6.5	−31.67	7.3

Notes: average wind power is 1218 MW. Average solar and wave power is 500 MW.

For the aggregate load, both capacity-up and capacity-down reserves average 59 MW, or slightly less than 1 percent of the power.

For wind, capacity-up reserves are as high as 161 MW, or 16 percent of power, while capacity-down reserves are estimated at −94 MW, or 37 percent of power. The asymmetry in the numbers and the ratios − higher reserves, lower ratios to power – is explained by the fact that surpluses occur primarily during periods of low wind power, typically when wind is ramping up, while deficits occur more often during periods of high wind power, when wind power is ramping down.

For solar, both capacity-up reserves and capacity-down reserves are in the range of 67 MW. Both values are in the range of 15–67 percent of power, comparable to capacity-up reserves for wind.

For waves, capacity-up reserves range from as little as 28.7 MW for the Pelamis to 31 MW for the heaving converter and 36 MW for the oscillating flap device. Expressed as ratios to power, these values are 5.6, 4.9 and 6.5 percent, much smaller than for wind and solar. Capacity-down reserves are even lower, −25.3, −26.3 and −31.7 MW for the three types of devices. The ratios to power are 5.9, 5.2 and 7.3 percent respectively.

7. Conclusions

Two conclusions emerge from this analysis. First, geographic dispersal of renewable energy generators tends to average out the localized noise, making the power easier to forecast. This is true for both waves and solar. One further implication of this finding is that physics-based wave models may be uniquely well-suited to wave farm simulation. Comparisons of physics model hindcasts with individual buoy data have generally found that the models produce much smoother values for the wave parameters [53,54]. However, since wave farms will be more dispersed than individual buoys, physics model hindcasts can be used to reproduce the wave parameters over wider areas.

Second, wave power remains much easier to forecast than either wind or solar. For wind power, the main issue for the forecaster is anticipating the large ramp events. For solar energy, the main problems are cloud cover and precipitation. While the wave energy flux can be extremely volatile, the power output from wave farms is smoother and more predictable. The main cause is geographic dispersal, but a second factor is that the converters cut off energy above a given threshold, mitigating the impact of extreme fluctuations. When the costs are expressed in terms of reserves, waves are far less expensive than other forms of renewable energy. The findings argue strongly for the development of wave energy at coastal locations.

Acknowledgments

The authors thank Frank Vignola of Oregon State University and Edwin Campos of Argonne National Laboratory for their assistance in obtaining the solar databases.

References

[1] Arinaga RA, Cheung KF. Atlas of global wave energy from 10 years of reanalysis and hindcast data. Renew Energy 2012;39:49–64.
[2] Esteban M, Leary D. Current developments and future prospects of off shore wind and ocean energy. Appl Energy 2011;90:128–36.
[3] Bonneville Power Administration, 2015. Website: www.bpa.gov. Wind and load data are available at: http://transmission.bpa.gov/Business/Operations/Wind/ Maps of the wind farms are available at: http://www.bpa.gov/transmission/Projects/wind-projects/Documents/bpa-wind-map.pdf and at http://www.bpa.gov/transmission/Projects/wind-projects/Pages/default.aspx.
[4] University of Oregon, Solar Radiation Laboratory, 2015. http://solardata.uoregon.edu.
[5] Electric Power Research Institute (EPRI). Mapping and assessment of the United States ocean wave energy resource. 2011 Technical Report. 2011.
[6] National Data Buoy Center, 2015. www.ndbc.noaa.gov.
[7] European Center for Medium-range Weather Forecasts, 2015. www.ecmwf.int The wave model is available at: http://www.ecmwf.int/en/research/modelling-and-prediction/marine.
[8] Hasselmann K, Ross DB, Müller P, Sell W. A parametric wave prediction model. J Phys Oceanogr 1976;6:200–28.
[9] Hasselmann DE, Dunckel M, Ewing JA. Directional wave spectra observed during JONSWAP 1973. J Phys Oceanogr 1980;10:1264–80.
[10] Hasselmann S, Hasselmann K, Allender JH, Barnett TP. Computations and parameterizations of the non-linear energy transfer in a gravity wave spectrum. Part II: parameterizations of the non-linear energy transfer for application in wave models. J Phys Oceanogr 1985;15:1378–91.
[11] Janssen PAEM. Quasi-linear theory of wind-wave generation applied to wave forecasting. J Phys Oceanogr 1991;21:1631–42.
[12] Janssen PAEM. Progress in ocean wave forecasting. J Comput Phys 2007;227:3572–94.
[13] Parkinson S, Dragoon K, Reikard G, Ozkan-Haller HT, Brekken TKA. Integrating ocean wave energy at large scales: a study of the Pacific Northwest. Renew Energy 2015;76:551–9.
[14] Reikard G. Integrating wave energy into the power grid: simulation and forecasting. Ocean Eng 2013;73:168–78.
[15] Retzler C. Measurements of the slow drift dynamics of a model Pelamis wave energy converter. Renew Energy 2006;31:257–69.
[16] Yemm R, Pizer D, Retzler C, Henderson R. Pelamis: experience from concept to connection. Philos Trans R Soc 2012;370:365–80.
[17] Henderson R. Design, simulation, and testing of a novel hydraulic power take-off system for the Pelamis wave energy converter. Renew Energy 2006;31:271–83.
[18] Pelamis. 2015. www.pelamiswave.com.
[19] Babarit A, Hals J, Muliawan MJ, Kurniawan A, Moan T, Krokstad J. Numerical benchmarking study of a selection of wave energy converters. Renew Energy 2012;41:44–63.
[20] Brekken TKA, Ozkan-Haller HT, Simmons A. A methodology for large-scale ocean wave power time-series generation. IEEE J Ocean Eng 2012;37:294–300.
[21] Bidlot JR, Holmes DJ, Wittmann PA, Lalbeharry R, Chen HS. Inter-comparison of the performance of operational ocean wave forecasting systems with buoy data. Weather Forecast 2002;17:287–310.
[22] Roulston MS, Ellepola J, von Hardenberg J, Smith LA. Forecasting wave height probabilities with numerical weather prediction models. Ocean Eng 2005;32:1841–63.
[23] Mathiesen P, Collier C, Kleissl J. A high-resolution, cloud-assimilating numerical weather prediction model for solar irradiance forecasting. Sol Energy 2013;92:47–61.
[24] Cutler NJ, Outhred HR, MacGill IF, Kay MJ, Kepert JD. Characterizing future large, rapid changes in aggregated wind power using numerical weather prediction spatial fields. Wind Energy 2009;12:542–55.
[25] Cutler NJ, Outhred HR, MacGill IF, Kepert JD. Predicting and presenting plausible future scenarios of wind power production from numerical weather prediction systems: a qualitative ex ante evaluation for decision making. Wind Energy 2011;15:473–88.

[26] Reikard G, Pinson P, Bidlot JR. Forecasting ocean wave energy: the ECMWF wave model and time series methods. Ocean Eng 2011;38:1089–99.
[27] Pinson P, Reikard G, Bidlot JR. Probabilistic forecasting of the wave energy flux. Appl Energy 2012;93:364–70.
[28] Marquez R, Coimbra CFM. Forecasting of global and direct solar irradiance using stochastic learning methods, ground experiments and the NWS database. Sol Energy 2011;85:746–56.
[29] Perez R, Kivalov S, Schlemmer J, Hemker K, Renne D, Hoff TE. Validation of short and medium term operational solar radiation forecasts in the US. Sol Energy 2010;84:2161–72.
[30] Pinson P, Nielsen HA, Moller JK, Madsen H, Karinotakis GN. Non-parametric probabilistic forecasts of wind power: required properties and evaluation. Wind Energy 2007;10:497–516.
[31] Yoder M, Hering AS, Navidi WC, Larson K. Short-term forecasting of categorical changes in wind power with Markov chain models. Wind Energy 2013;17:1425–39.
[32] Bunn DW. Modelling prices in competitive electricity markets. New York: Wiley; 2004.
[33] Granger CWJ. Non-linear models: where do we go next – time varying parameter models? Stud Nonlinear Dyn Econ 2008;12. Article 1, http://www.bepress.cxom/snde/vol12/iss3/art1.
[34] Akaike H. Information theory and the extension of the maximum likelihood principle. In: Petrov BN, Csaki F, editors. Second International Symposium on Information Theory. Budapest: Akademiai Kiado; 1973. p. 267–81.
[35] Cao JJ, Cao SH. Study of forecasting solar irradiance using neural networks with preprocessing sample data by wavelet analysis. Energy 2006;31:3435–45.
[36] Chen C, Duan S, Cai T, Liu B. Online 24-h solar power forecasting based on weather type classification using artificial neural network. Sol Energy 2011;85:2856–70.
[37] Deo MC, Jagdale SS. Prediction of breaking waves with neural networks. Ocean Eng 2003;30:1163–78.
[38] Deo MC, Naidu CS. Real time wave forecasting using neural networks. Ocean Eng 1998;26:191–203.
[39] Deo MC, Jha A, Chaphekar AS, Ravikant K. Neural networks for wave forecasting. Ocean Eng 2001;28:889–98.
[40] Paoli C, Voyant C, Muselli M, Nivet ML. Forecasting of preprocessed daily solar radiation time series using neural networks. Sol Energy 2010;84:2146–60.
[41] Londhe SN, Panchang V. One-day wave forecasts based on artificial neural networks. J Atmos Ocean Technol 2006;23:1593–603.
[42] Tsai CP, Lin C, Shen JN. Neural network for wave forecasting among multi-stations. Ocean Eng 2002;29:1683–95.
[43] Tseng CM, Jan CD, Wang JS, Wang CM. Application of artificial neural networks in typhoon surge forecasting. Ocean Eng 2007;34:1757–68.
[44] Box GEP, Jenkins GJ. Time series analysis, forecasting and control. San Francisco: Holden-Day; 1976.
[45] Kalman RE. A new approach to linear filtering and prediction problems. Trans Am Soc Mech Eng J Basic Eng 1960;83D:35–45.
[46] Rossi B, Inoue A. Out-of-sample forecast tests robust to the choice of window size. J Bus Econ Stat 2012;30:432–53.
[47] Reikard G. Using temperature and state transitions to forecast wind speed. Wind Energy 2008;11:431–43. http://dx.doi.org/10.1002/we/263.
[48] Reikard G. Regime-switching models and multiple causal factors in forecasting wind speed. Wind Energy 2010;13:407–18. http://dx.doi.org/10.1002/we.361.
[49] Reikard G. Predicting solar radiation at high resolutions: a comparison of time series forecasts. Sol Energy 2009;83:342–9. http://dx.doi.org/10.1016/j.solener.2008.08.07.
[50] Huang J, Korolkiewicz M, Agrawal M, Boland J. Forecasting solar radiation on an hourly time scale using a coupled autoregressive and dynamic system (CARDS) model. Sol Energy 2013;87:136–49.
[51] Zhang GP. Time series forecasting using a hybrid ARIMA and neural network model. Neurocomputing 2003;50:159–75.
[52] Order No. 764 Federal Energy Regulatory Center (FERC). Washington, DC: Federal Energy Regulatory Center; 2012.
[53] Chawla A, Spindler DM, Tolman HL. Validatino of a thirty year wave hindcast using the climate forecast system reananlysis winds. Ocean Model 2012;70:189–206.
[54] Garcia-Medina G, Ozkan-Haller HT, Ruggiero P, Oskamp J. An inner-shelf wave forecasting system for the U.S. Pacific Northwest. Weather Forecast 2013;28:681–703.